THE JOURNAL OF BIOLOGICAL CHEMISTRY VOL. 285, NO. 12, pp. 9124–9136, March 19, 2010

Potassium Channel Modulation by a Toxin Domain in Matrix Metalloprotease 23*[S]

Received for publication, October 2, 2009, and in revised form, December 1, 2009 Published, JBC Papers in Press, December 4, 2009, DOI 10.1074/jbc.M109.071266

Srikant Rangaraju[‡1], Keith K. Khoo[§¶1], Zhi-Ping Feng[§], George Crossley[‖], Daniel Nugent[‖], Ilya Khaytin[‖], Victor Chi[‡], Cory Pham[‡], Peter Calabresi[**], Michael W. Pennington[‖2], Raymond S. Norton[§2,3], and K. George Chandy[‡2,4]

From the [‡]Departments of Physiology and Biophysics and Pathology, University of California, Irvine, California 92697, the [§]Walter and Eliza Hall Institute of Medical Research, Parkville, Victoria 3052, Australia, the [¶]Department of Medical Biology, University of Melbourne, Parkville, Victoria 3010, Australia, [‖]Bachem Bioscience Inc., King of Prussia, Pennsylvania 19406, and the [**]Department of Neurology/Neurosurgery, The Johns Hopkins University School of Medicine, Baltimore, Maryland 21287

Peptide toxins found in a wide array of venoms block K^+ channels, causing profound physiological and pathological effects. Here we describe the first functional K^+ channel-blocking toxin domain in a mammalian protein. MMP23 (matrix metalloprotease 23) contains a domain ($MMP23_{TxD}$) that is evolutionarily related to peptide toxins from sea anemones. $MMP23_{TxD}$ shows close structural similarity to the sea anemone toxins BgK and ShK. Moreover, this domain blocks K^+ channels in the nanomolar to low micromolar range (Kv1.6 > Kv1.3 > Kv1.1 = Kv3.2 > Kv1.4, in decreasing order of potency) while sparing other K^+ channels (Kv1.2, Kv1.5, Kv1.7, and KCa3.1). Full-length MMP23 suppresses K^+ channels by co-localizing with and trapping $MMP23_{TxD}$-sensitive channels in the ER. Our results provide clues to the structure and function of the vast family of proteins that contain domains related to sea anemone toxins. Evolutionary pressure to maintain a channel-modulatory function may contribute to the conservation of this domain throughout the plant and animal kingdoms.

Mechanisms that fine tune the activity of potassium channels are crucial to a cell's ability to integrate and respond to a plethora of internal and external signals. Peptide toxins from venomous creatures have served as vital tools to define the molecular mechanisms underlying K^+ channel function (1, 2). It has been suggested that toxins evolved from endogenous genes that function in normal cellular pathways (3, 4). Indeed, venomous creatures possess toxins with homology to several proteins, including acetylcholinesterases (5), phospholipases (6, 7), nerve growth factor (8), endothelins (9), Lynx-1 (10, 11), Kunitz-type serine protease inhibitors (12), and the ion channel regulatory (ICR)[5] domains of cysteine-rich secretory proteins (CRISPs) (3, 13, 14). Mammalian proteins containing toxin-like domains (TxDs) that block K^+ channels have not been characterized previously.

BgK, a 37-residue peptide toxin from the sea anemone *Bunodosoma granulifera* (15, 16), and ShK, a 35-residue peptide toxin from the sea anemone *Stichodactyla helianthus* (17, 18) are potent inhibitors of K^+ channels. The Simple Modular Architecture Research Tool (SMART) (available on the World Wide Web) predicts the existence of a large superfamily of proteins that contain domains (referred to as ShKT domains in the SMART data base) resembling these two toxins (Fig. 1*A*). Many of these proteins (~70 proteins) are metallopeptidases, whereas others are prolyl-4-hydroxylases, tyrosinases, peroxidases, oxidoreductases, or proteins containing epidermal growth factor-like domains, thrombospondin-type repeats, or trypsin-like serine protease domains (Fig. 1*B*). The only human protein containing a ShKT domain in the SMART data base is MMP23 (matrix metalloprotease 23). Matrix metalloproteases belong to the metzincin superfamily and play important roles in tissue remodeling, development, and the immune response (19).

MMP23 is expressed in many tissues and exists either as a type II transmembrane protein in ER/nuclear membranes or as a secreted form following cleavage of the RRRRY motif just N-terminal to the Zn^{2+}-dependent metalloprotease domain (20–23). The ShKT domain of MMP23 ($MMP23_{TxD}$) lies between the metalloprotease domain and an immunoglobulin-like cell adhesion molecule (IgCAM) domain (Fig. 2*A*). MMP23 has been implicated in prostate, brain, and breast cancer (24–26). In humans, two related sequences, MMP23A (a pseudogene) and MMP23B, are co-located on chromosome 1p36 (20). We have investigated MMP23 to gain insight into the structure and physiological functions of ShKT toxin domains and describe the solution structure of the $MMP23_{TxD}$ domain, its

* This work was supported, in whole or in part, by National Institutes of Health Grants NS-048252 (to K. G. C. and M. W. P.) and NS041435 (to P. C. and K. G. C.). This work was also supported by National Health and Medical Research Council Independent Research Institutes Infrastructure Support Schemes Grant 361646 (to R. S. N.) and a Victorian State Government Operational Infrastructure Support grant (to R. S. N.).

[S] The on-line version of this article (available at http://www.jbc.org) contains supplemental Tables S1–S4 and Figs. S1–S6.

The atomic coordinates and structure factors (code 2K72) have been deposited in the Protein Data Bank, Research Collaboratory for Structural Bioinformatics, Rutgers University, New Brunswick, NJ (http://www.rcsb.org/).

The chemical shift data reported in this paper have been submitted to the BioMagResBank Data Bank with the accession number(s) 15900.

[1] Both authors contributed equally to this work.

[2] These authors contributed equally to this work.

[3] Supported by a fellowship from the National Health and Medical Research Council.

[4] To whom correspondence should be addressed: Dept. of Physiology and Biophysics, 291 JISH, School of Medicine, University of California Irvine, Irvine, CA 92697. Fax: 949-824-3143; E-mail: gchandy@uci.edu.

[5] The abbreviations used are: ICR, ion channel regulatory; CRISP, cysteine-rich secretory protein; TxD, toxin-like domain; Fmoc, *N*-(9-fluorenyl)methoxycarbonyl; IgCAM, immunoglobulin-like cell adhesion molecule; RP, reverse phase; HPLC, high pressure liquid chromatography; NOE, nuclear Overhauser effect; ER, endoplasmic reticulum; r.m.s., root mean square; eGFP, enhanced green fluorescent protein.

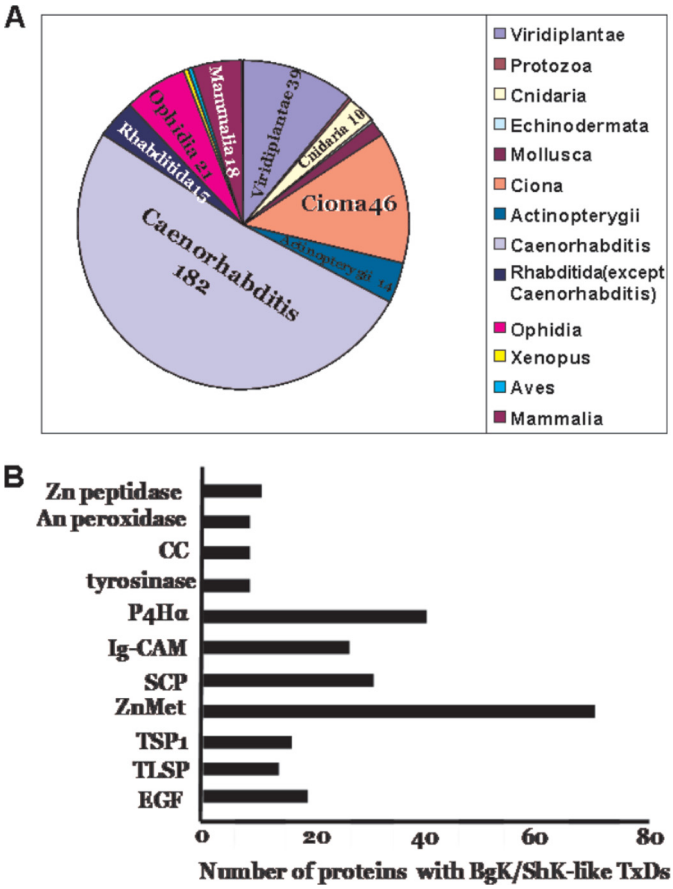

FIGURE 1. **The ShKT domain protein superfamily.** *A*, distribution of ShKT domains in the plant and animal kingdoms. *Viridiplantae*, *Arabidopsis thaliana*, *Oryza sativa*, and green alga *Ostreococcus* sp.; *Protozoa*, *Cryptosporidium parvum*; *Cnidaria*, sea anemones, hydra, and jellyfish; *Echinodermata*, sea urchin; *Mollusca*, includes bivalve clams and oysters; *Ciona*, sea squirt *Ciona intestinalis*; *Actinopterygii*, includes zebrafish *Danio rerio* and pufferfish *Takifugu rubripes*; *Caenorhabditis*, *C. elegans* and *Caenorhabditis brigssae*; *Rhabditida*, rhabditid nematodes other than *Caenorhabditis* sp.; *Ophidia*, snakes; *Xenopus*, *Xenopus tropicalis*; *Aves*, chicken *Gallus gallus*; *Mammalia*, kingdom mammalia. Data were generated from the SMART data base at the EMBL-Heidelberg. *B*, types of proteins containing ShKT domains. These include zinc peptidases (*Zn peptidase*), animal peroxidases (*An peroxidase*), coiled-coil regions (*CC*), tyrosinases, prolyl-4-hydroxylases (*P4Hα*), IgCAM domains, sperm-coating glycoprotein domains (*SCP*), zinc metalloproteases (*ZnMet*), thrombospondin type 1 repeats (*TSP1*), trypsin-like serine proteases (*TLSP*), and epidermal growth factor-like domains (*EGF*).

structural similarity to the sea anemone toxins BgK and ShK, and its functional role in blocking K^+ channels.

EXPERIMENTAL PROCEDURES

Synthesis and Purification of MMP23$_{TxD}$—We synthesized the 37-residue rat MMP23$_{TxD}$ on Ramage^{TM} resin using an automated protocol. Fmoc-amino acids (Bachem AG) included Arg(2,2,5,7,8-pentamethylchroman-6-sulfonyl), Asp(tributyl ester), Cys(trityl), Gln(trityl), His(trityl), Lys(*t*-butoxycarbonyl), Ser(*t*-butyl), Thr(*t*-butyl), Trp(*t*-butoxycarbonyl), and Tyr(*t*-butyl). Stepwise assembly was carried out on a 0.25-mmol scale on a Symphony automated peptide synthesizer using *O*-benzotriazole-*N*,*N*,*N*′,*N*′-tetramethyluronium hexafluorophosphate activation and standard Fmoc-solid phase peptide synthesis methods. Following chain assembly, 800 mg of resin was cleaved using reagent K/trifluoroacetic acid (1:9) for 2 h at room temperature (27). Resin was filtered, and the peptide was precipitated using diethyl ether. The yield was 350 mg of peptide.

The peptide was prepurified to ~75% using preparative RP-HPLC (Kromasil-C18 10u) and lyophilized. Purification of 250 mg yielded 40 mg of semipure material, which was folded by dissolving the reduced and prepurified peptide in DMSO and then diluting to 0.25 mg/ml with 10% DMSO, 10% isopropyl alcohol, 2 M guanidine HCl and adjusting the pH to 7.6 with NH_4OH. The solution, which remained clear during the pH adjustment, was then allowed to oxidize overnight. Liquid chromatography-mass spectrometry samples were taken at 2, 4, 6, and 24 h. Two peaks with the correct mass formed initially, but with longer reaction times, one peak became dominant. After 36 h, the folding was stopped by acidifying the solution with HCl to a pH of 4.0. The solution was diluted 50% with H_2O and filtered before preparative HPLC purification over an reverse phase high performance liquid chromatography C18 column using a gradient of 15–45% B in 45 min (buffers A and B were 0.1% trifluoroacetic acid in H_2O and acetonitrile, respectively). Mass spectral analysis determined the (M + H) to be 4427, consistent with the formation of three intramolecular disulfide bonds. The final yield of 26 mg was at a purity of 95%.

NMR Spectroscopy—Synthetic MMP23$_{TxD}$ (6 mg) was dissolved in 600 μl of H_2O containing 6% ^2H_2O, and the pH was adjusted to 5.0. Two-dimensional homonuclear total correlation (TOCSY) spectra with a spin-lock time of 70 ms, nuclear Overhauser enhancement (NOESY) spectra with mixing times of 250, 150, and 50 ms, and double quantum-filtered correlation (DQF-COSY) spectra were acquired at 600 MHz on a Bruker DRX-600 spectrometer. Spectra were acquired at 20 °C unless otherwise stated and referenced to dioxane (3.75 ppm). TOCSY and NOESY spectra were also collected at 5 °C. The water resonance was suppressed using the WATERGATE pulse sequence (28, 29). A series of one-dimensional spectra over the temperature range 5–25 °C, at 5 °C intervals, was collected. Amide exchange rates were monitored by dissolving freeze-dried material in ^2H_2O at pH 5.2 and then recording a series of one-dimensional spectra, followed by 70-ms TOCSY, 50-ms NOESY, and an exclusive correlation (E-COSY) spectra, all at 5 °C. In addition, ^1H-^{13}C HSQC spectra for the assignment of ^{13}C chemical shifts and a ^1H-^{15}N HSQC spectrum for the assignment of ^{15}N chemical shifts (28, 30, 31) were collected at 20 °C on the Bruker DRX-600 and a Bruker Avance 500 spectrometer equipped with a TXI-cryoprobe, respectively. Diffusion measurements were performed at 5 and 20 °C using a pulsed field gradient longitudinal eddy-current delay pulse sequence (31, 32) as implemented (33). Spectra were processed using TOPSPIN (version 1.3, Bruker Biospin) and analyzed using XEASY (version 1.3.13) (34).

Structural Constraints—$^3J_{HNHA}$ coupling constants were measured from DQF-COSY spectra at 600 MHz and then converted to dihedral restraints as follows: $^3J_{HNH\alpha} > 8$ Hz, $\phi = -120 \pm 40°$; $^3J_{HNH\alpha} < 6$ Hz, $\phi = -60 \pm 30°$. χ^1 angles for some residues were determined based on analysis of a short mixing time (50 ms) NOESY spectrum. In addition, TALOS (35) was used to predict torsion angle (ϕ and ψ) restraints based on chemical shifts. Predicted ϕ and ψ angles of residues that gave good prediction scores (17 residues: 12–16, 22–25, and 27–34) were constrained (range ± 40°) in structural calculations in

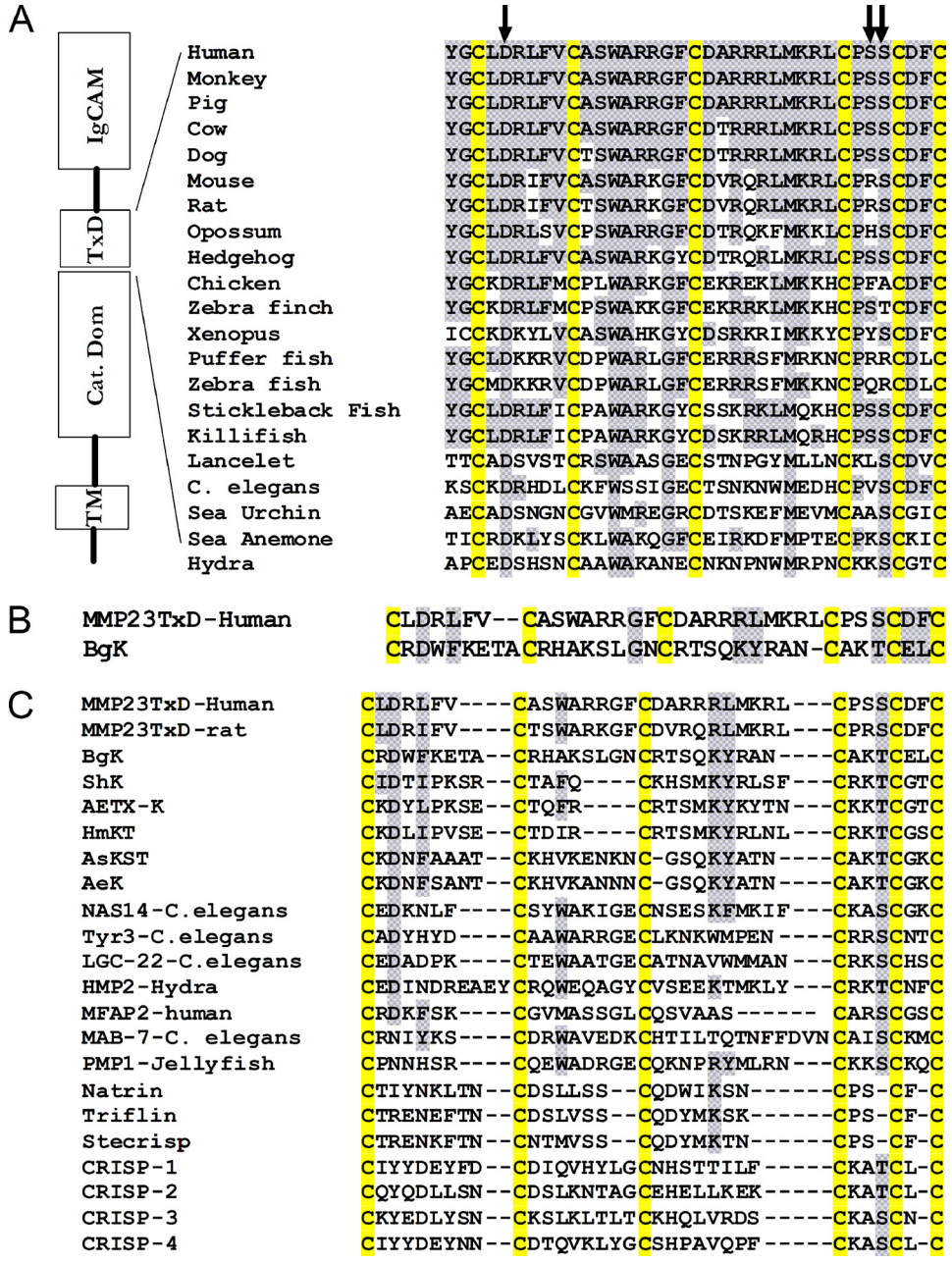

FIGURE 2. **MMP23 aligned with sea anemone toxins, representative ShKT domains, and ICR domains of CRISPs.** *A*, schematic diagram of MMP23 showing $MMP23_{TxD}$ *sandwiched between* the metalloprotease and IgCAM domains. A multiple protein sequence alignment of $MMP23_{TxD}$s from diverse species is shown. Cysteine residues are highlighted in *yellow*. Identical or synonymous sequences are highlighted in *gray*. The *arrows* point to Asp^5, Ser^{32}, and Ser^{33}. *B*, protein sequence alignment of human $MMP23_{TxD}$ and BgK. *C*, multiple sequence alignment of representative ShKT domains together with the ICR domains of CRISPs. Cysteine residues are highlighted in *yellow*. Identical or synonymous sequences are highlighted in *gray*. Sea anemone toxins include BgK (accession number P29186), ShK (accession number P29187), AeTX-K (accession number Q0EAE5), AsKS (accession number Q9TWG1), AeK (accession number P81897), and HmKT (accession number O16846). *NAS14-C. elegans*, nematode astacin metalloprotease NAS14 (accession number Q19269). *Tyr3-C. elegans*, tyrosinase 3 (accession number Q19673). *LGC-22-C. elegans*, ligand-gated channel 22 (accession number NP_500538). *HMP2-Hydra*, Hydra metalloprotease 2 (accession number AAD33860). *MFAP2-human*, microfibril associated protein 2 (accession number P55001). *MAB-7*, male abnormal protein 7 (accession number NP_508174). *PMP1-Jellyfish*, *Podocoryne* metalloproteinase 1 (58).

XPLOR. Two χ^1 angles (Asp^5 and Phe^{36}) were constrained in final structure calculations. The number of final dihedral angle constraints is listed in supplemental Table S1, and details have been deposited along with distance constraints in BioMagResBank (36) as entry 15900. Because disulfide bonds for $MMP23_{TxD}$ had not been mapped, these were not included as structural restraints in preliminary calculations. Subsequently, disulfide bond connectivities were determined based on Cys_AH^{α}-Cys_BH^{β} and Cys_AH^{β}-Cys_BH^{β} intercysteine NOEs observed in NOESY spectra (37) as well as Cys_AC^{β}–Cys_BC^{β} and Cys_AS^{γ}–Cys_BS^{γ} intercysteine distance calculations in preliminary structures (supplemental Table S4). Disulfide bonding was determined to be Cys^3-Cys^{37}, Cys^{10}-Cys^{30}, Cys^{19}-Cys^{34}, which is the same pattern as in ShK and BgK. These were added as restraints for final structure calculations. No hydrogen bond restraints were included.

Structure Calculations—Intensities of NOE cross-peaks were measured in XEASY and calibrated using the CALIBA macro of the program CYANA (version 1.0.6) (38). NOEs providing no restraint or representing fixed distances were removed. The constraint list resulting from the CALIBA macro of CYANA was used in XPLOR-NIH to calculate a family of 200 structures using the simulated annealing script (39). The 55 lowest energy structures were then subjected to energy minimization in water; during this process, a box of water with a periodic boundary of 18.856 Å was built around the peptide, and the ensemble was energy-minimized based on NOE and dihedral restraints and the geometry of the bonds, angles, and impropers. From this set of structures, final families of 20 lowest energy structures were chosen for analysis using PROCHECK-NMR (40) and MOLMOL (41). In all cases, the final structures had no experimental distance violations of >0.2 Å or dihedral angle violations of >5°. The structures have been deposited in the Protein Data Bank (42) with code 2K72. Structural figures were prepared using the programs MOLMOL (41) and PyMOL (DeLano Scientific, San Carlos, CA).

Cell Lines, Transfection, and Cell Culture—Stable cell lines expressing K^+ channels (43) were used for electrophysiology. Kv1.6 (in pcDNA3.1) was transiently transfected with pEGFP-C1 in COS7 cells for 24–30 h. COS7 cells were grown

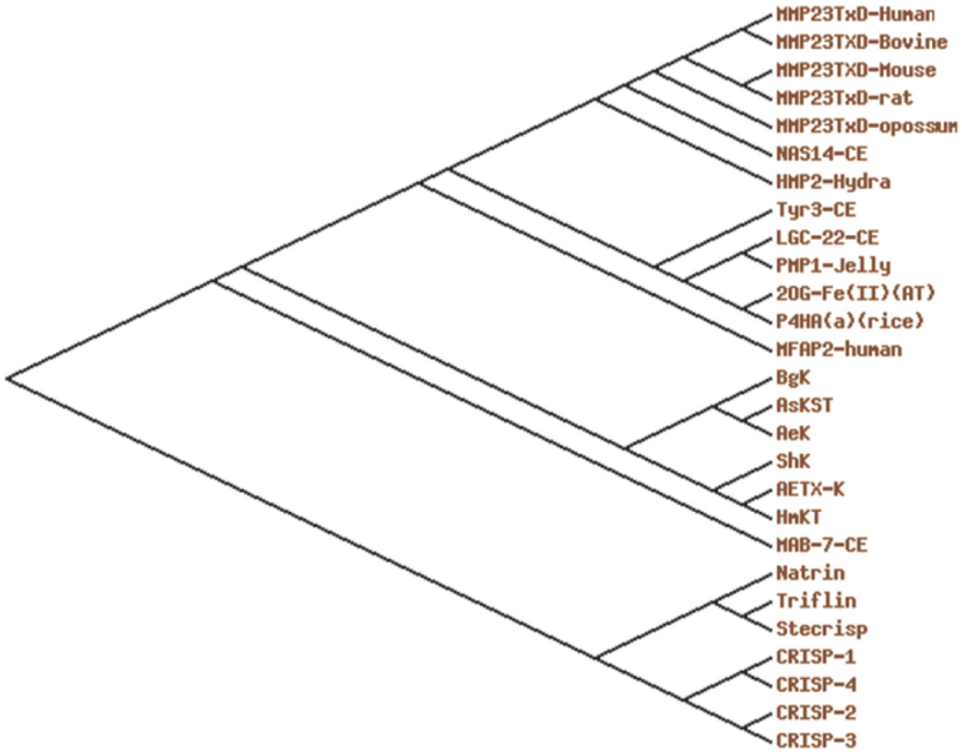

FIGURE 3. **Evolutionary relationships of $MMP23_{TxD}$ with sea anemone toxins, ShKT domains, and ICR domains of CRISPs.** A phylogenetic tree (PHYLIP) was generated using the alignment in Fig. 2*C* and the GeneBee Molecular Biology Servers Tree Top Phylogenetic tree prediction algorithm. In addition to the protein sequences used in the multiple sequence alignment in Fig. 2*C*, two plant proteins are included in the phylogenetic tree: oxidoreductase, 2OG-Fe(II) oxygenase family protein from *A. thaliana* (accession number NP_189490) and prolyl-4-hydroxylase α-subunit, *O. sativa japonica* group (accession number AAT77286).

to 60–80% confluence in 6-well culture plates and were transfected with 0.4–1 μg of DNA using Lipofectamine 2000 (Invitrogen) in Opti-MEM I medium as per the manufacturer's protocol. After 24–30 h, transfection efficiency was assessed by fluorescence microscopy (Olympus).

eGFP-MMP23 was generated using the following PCR primers: 5′ primer, 5′-CCCAAGCTTCCATGGGATGGCGAGCATGTCTCCGTCCGGAGGCGTC-3′; 3′ primer, 5′-GATGGATCCGAATTCTCAGCTCCTCACTCGGACCCTCCAGGA-3′. Two-step PCR amplification was performed using rat MMP23 cDNA as template (Open Biosystems). The 1200-bp PCR product was inserted into pEGFP-C1 (Clontech) at 5′ HindIII and 3′ BamHI restriction sites. The ligated product was transformed into XL1-blue *Escherichia coli*. The purified construct was used for transient transfection after sequence confirmation. pEGFP-C1 or pEGFP-MMP23 along with hKv1.3 or hKv1.6 cDNA (in pcDNA3.1) were also co-transfected into COS7 cells (ratio 8:1), which were then trypsinized after 24 h, plated on coverslips, and followed by electrophysiological studies. Fluorescent cells were patch-clamped for outward potassium currents. Stable cell lines expressing Kv1.2, Kv1.7, and Kv1.3 were transfected with pEGFP-C1 or pEGFP-MMP23 for suppression experiments. Expression of constructs in COS7 cells was confirmed by Western blot.

Electrophysiology—All experiments were conducted in the whole-cell configuration of the patch clamp technique, as described previously (1, 43, 44). Data acquisition and analysis was performed using pClamp software.

Immunostaining and Confocal Microscopy—COS7 cells transiently co-transfected with eGFP or eGFP-MMP23 and hKv1.3, or Kv1.2-expressing cells transfected with eGFP-C1 or eGFP-MMP23, were allowed to stick to poly-L-lysine (Sigma)-coated coverslips for 1 h prior to fixing (2% paraformaldehyde (Sigma)) and permebilization (0.1% Triton X-100 in phosphate-buffered saline). Coverslips were blocked overnight with 5% bovine serum albumin plus 5% goat serum in phosphate-buffered saline. Cells were incubated with primary rabbit polyclonal anti-Kv1.3 antibodies (gift from Dr. Hans Gunther Knaus) (1:1000) for 2 h followed by secondary anti-rabbit IgG-Alexa 647 (Molecular Probes) for 1 h. For ER co-localization experiments, COS7 cells transfected with EGFP-C1 or eGFP-MMP23 were stained with anti-SERCA2 monoclonal antibody (1:1000; Molecular Probes) and secondary anti-mouse IgG-Alexa 647 (1:1000; Molecular Probes). Nonspecific rabbit IgG controls were performed for each experiment. All incubations were performed in the dark. Cells were imaged by confocal microscopy (LSM Zeiss Meta 2). Images were analyzed for co-localization using LSM 510 software (n = 3 independent experiments; 20–30 cells were imaged for quantification of co-localization).

For flow cytometric studies to determine surface Kv1.3 channels using ShK-F6CA, the MMP23 construct from pEGFP-C1 was subcloned into pdsRED-C1 monomer (Clontech) at 5′ HindIII and 3′ BamHI restriction sites. We then co-transfected COS7 cells with human Kv1.3 and pDsRED-C1 (Clontech) or pDsRED-MMP23 for 30 h. Cells were trypsinized and incubated with 10 nM ShK-F6CA (44) in phosphate-buffered saline plus 2% goat serum for 30 min and were then washed three times with phosphate-buffered saline plus 2% goat serum. The intensity of ShK-F6CA staining (a measure of Kv1.3 cell surface expression) was determined by flow cytometric analysis (FACSCalibur flow cytometer and BD CellQuest Pro software, BD Biosciences). The D value, a measure of the difference in mean fluorescence intensities (MFI) of stained and unstained cells, was calculated as follows.

$$D = (MFI_{Stained\ cells} - MFI_{Unstained\ cells})/MFI_{Unstained\ cells} \quad \text{(Eq. 1)}$$

RESULTS

Phylogenetic Relatedness of ShKT Domain-containing Proteins—The MMP23 ShKT domains (henceforth referred to as $MMP23_{TxD}$) from humans to hydra exhibit remarkable sequence conservation with no gaps or insertions in the domain (Fig. 2*A*). We compared the $MMP23_{TxD}$ sequence with that of

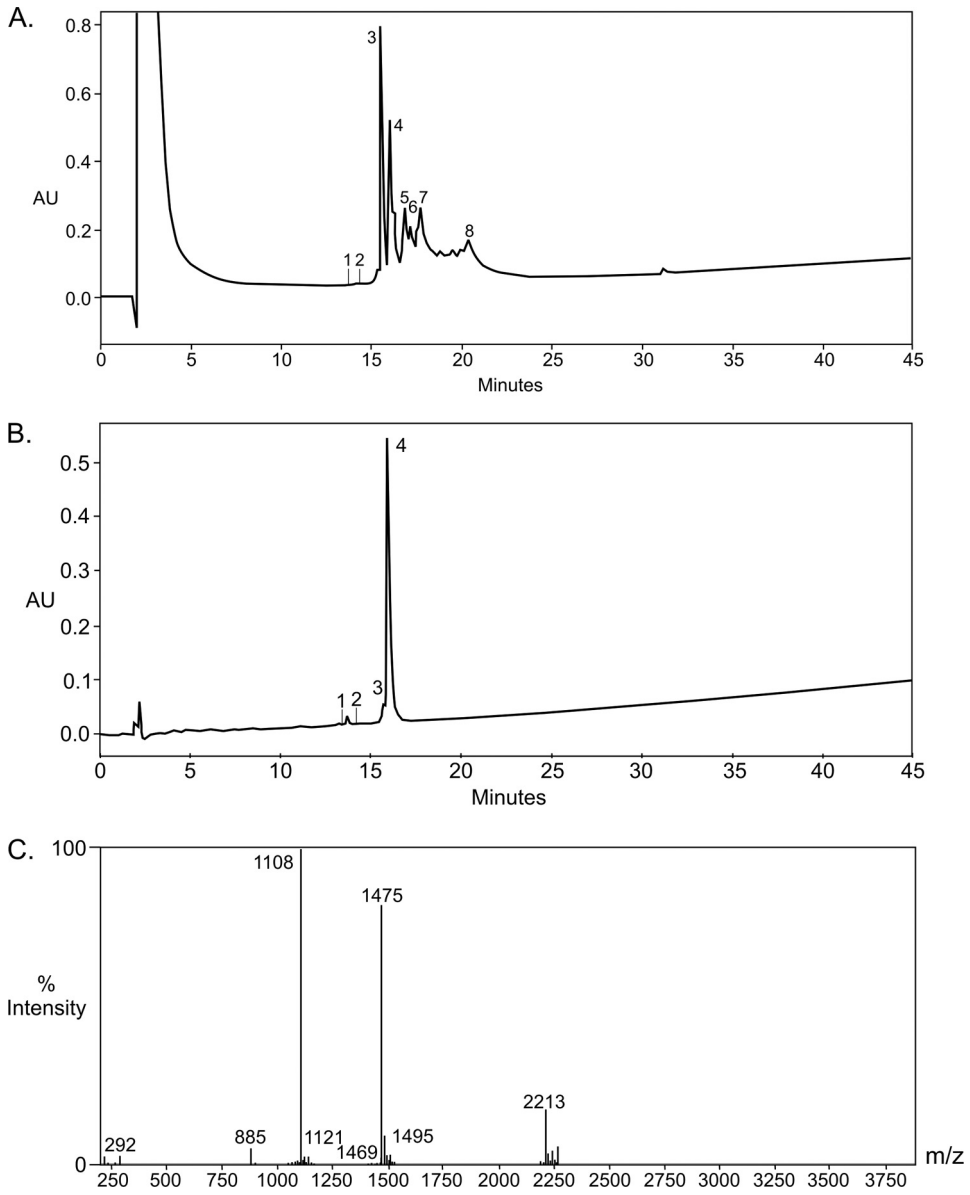

FIGURE 4. **Synthesis of $MMP23_{TxD}$ peptide.** *A*, RP-HPLC profile after 24 h of oxidative folding. A gradient of 5–95% B in 45 min was used (1.5 ml/min), where A is 0.1% trifluoroacetic acid in water and B is 0.1% trifluoroacetic acid in acetonitrile. *Peak 3* is $MMP23_{TxD}$. *B*, purified $MMP23_{TxD}$ RP-HPLC profile with the same gradient parameters. *Peak 4* is the correctly folded material. *C*, electrospray mass spectrum of $MMP23_{TxD}$ with M + 5 = 885, M + 4 = 1108, M + 3 = 1475, and M + 2 = 2213 peaks indicated. *AU*, absorbance units.

sea anemone toxins as well as representative members of the ShKT domain family from worms, cnidarians, and plants (Fig. 2, *B* and *C*). We included in the sequence alignment a second human protein, microfibril associated protein MFAP2, with an ShKT domain that is not mentioned in the SMART data base (45). Because the ICR domains of CRISPs share structural similarity with ShKT domains (46–50), we also included snake and human ICR domain sequences.

When compared with sea anemone toxins, $MMP23_{TxD}$s appear most similar to BgK with identical or equivalent substitutions at 14 of 36 positions (Fig. 2*B*). Asp^5 is conserved in all members of the ShKT domain family but is absent in the ICR domains of CRISPs (Fig. 2*C*). In ShK, the carboxylate of this aspartate (Asp^5 in ShK) forms a salt bridge with the ϵ-ammonium group of Lys^{30}, and this salt bridge is necessary for proper folding of the peptide (18, 51, 52). Lys^{32} and Arg^{32} at the equivalent position in $MMP23_{TxD}$s from sea anemone, hydra, rat, mouse, and puffer fish (Fig. 2*A*) could form a salt bridge with the aspartate. Other $MMP23_{TxD}$s contain Ser^{32} (Fig. 2*A*), and in these domains, Asp^5 may make hydrogen bonding interactions with the side chain hydroxyl or the peptide backbone. In the multiple sequence alignment, most proteins, with the exception of the three snake CRISPs, contain a serine or threonine at position 33 (Fig. 2*C*).

All sea anemone toxins contain a lysine residue (Lys^{25} in BgK, Lys^{22} in ShK) that occludes the K^+ channel pore (16, 51–54). Replacement of this residue with alanine abolishes K^+ channel blocking activity, whereas replacement with shorter or longer chained positively charged residues retains activity, albeit with lower potency (51–54). Four $MMP23_{TxD}$s (opossum, chicken, zebra finch, stickleback fish) contain lysine at the corresponding position, whereas other vertebrate $MMP23_{TxD}$s contain arginine (Fig. 2*A*). Interestingly, ICR domains of three snake CRISPs (natrin, triflin, and stecrisp) possess the critical pore-occluding lysine (Fig. 2*C*), and natrin has been reported to block the voltage-gated Kv1.3 channel (46). The ICR domains of the four mammalian CRISP proteins contain Thr, Leu, or Ala at the corresponding position (Fig. 2*C*) and therefore may not block K^+ channels. One of these, CRISP-2/Tpx-1, has been reported to block ryanodine receptors (13).

A phylogenetic tree based on the multiple sequence alignment of representative proteins from the ShKT domain family and generated with the PHYLIP program (available at the GeneBee Web site) places the $MMP23_{TxD}$s, the sea anemone toxins and the ICR-CRISP domains in distinct but related clades (Fig. 3). $MMP23_{TxD}$s also show phylogenetic relatedness to ShKT domains in MFAP2 (45); *Caenorhabditis elegans* proteins (astacin metalloprotease NAS14, tyrosinase Tyr3, ligand-gated channel lgc22, and Mab7 (56)) hydra and jellyfish astacin metalloproteases (HMP2 and PMP1 (57, 58)); and plant oxidoreductases (2OG-Fe(II)) and prolyl-4-hydroxylases (Fig. 3). TxDs in MMP23 and ICR domains of CRISPs are each encoded by a single exon (supplemental Fig. S1), raising the possibility that an ancient exon gave rise to these domains. Sea anemones may have

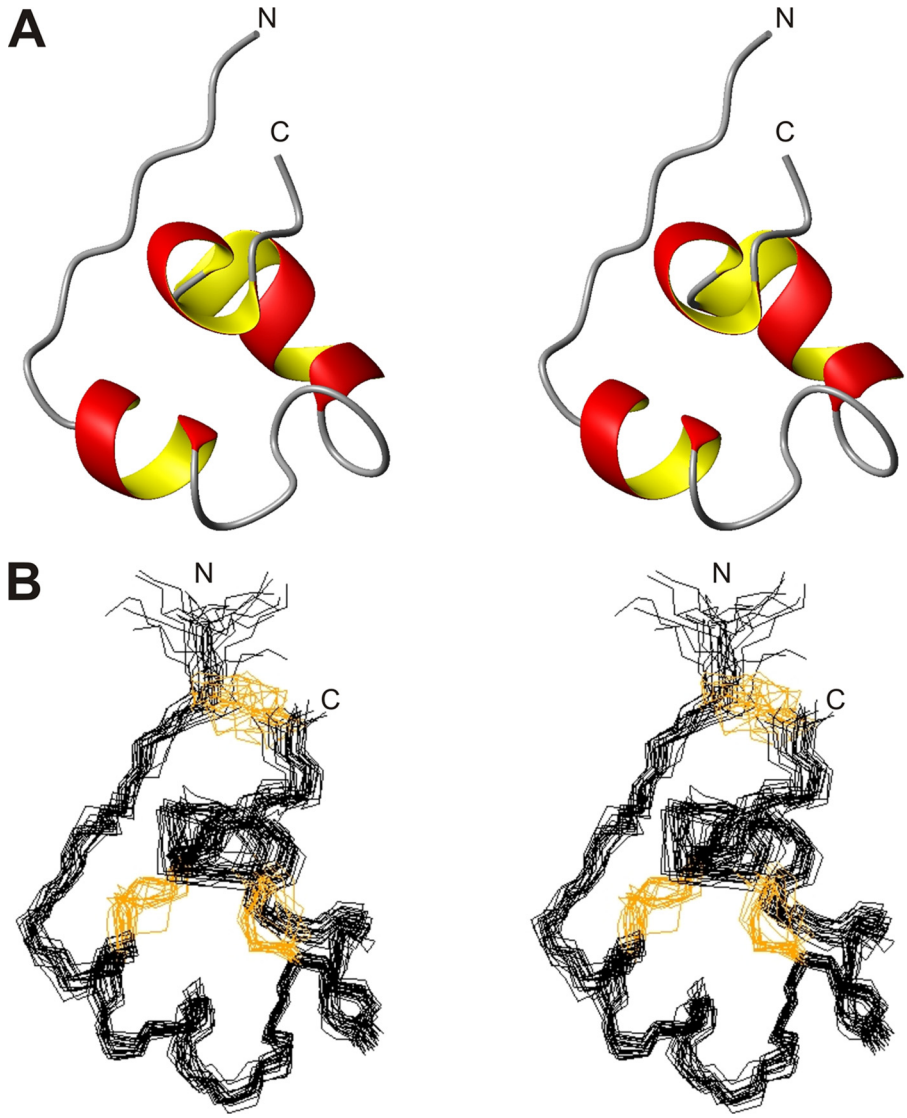

FIGURE 5. **Structure of MMP23$_{TxD}$.** *A*, stereo views of closest to average structure of MMP23$_{TxD}$ in *ribbon form* showing secondary structure. *N* and *C*, N and C termini, respectively. *B*, family of 20 final structures superimposed over backbone heavy atoms (N, C$^{\alpha}$, C′) over all residues with disulfide bonds shown in *orange*.

co-opted and modified this exon to generate potent K^+ channel-blocking toxins.

Synthesis of MMP23$_{TxD}$—We synthesized the 37-residue MMP23$_{TxD}$ on Ramage^{TM} amide resin with an automated Fmoc/tert-butyl protocol. Following cleavage and deprotection, 36 h was allowed for folding and oxidative formation of three disulfide bonds under conditions similar to those used for ShK. Folding proceeded smoothly to a major product that was homogeneous by analytical RP-HPLC (Fig. 4). Electrospray ionization mass spectral analysis yielded an (M + H) of 4427.33, consistent with the theoretical value following formation of three disulfide bonds (Fig. 4).

Solution Structure of MMP23$_{TxD}$—Details of the solution structure of MMP23$_{TxD}$ are provided in the supplemental material (supplemental Figs. S2–S6). A summary of experimental constraints and structural statistics for MMP23$_{TxD}$ is given in supplemental Tables S1–S4. The angular order parameters for Φ and ψ angles in the final ensemble of 20 structures were both >0.8 for residues 4–36. The mean pairwise r.m.s. deviation over the backbone heavy atoms of residues 4–36 in this family of structures was 0.75 Å. Three short α-helices encompassing residues 10–14, 23–29, and 31–34 characterize the closest to average structure of MMP23$_{TxD}$. Hydrogen bonds between Ala^{14} NH and Cys^{10} O, Lys^{16} NH and Trp^{13} O, and Leu^{25} NH and Arg^{22} O were observed in all 20 structures. The presence of medium-range $d_{\alpha N}(i,i+3)$ and $d_{\alpha N}(i,i+4)$ NOEs in these regions supports the helices observed. The conserved Asp^{5} is close to the guanidinium group of Arg^{32}, suggesting that a salt bridge or hydrogen bond may form between these two residues, as it does in sea anemone toxins. A stereo view of the closest to average structure of MMP23$_{TxD}$ is presented in Fig. 5*A*. The family of 20 final structures superimposed over the backbone heavy atoms (N, C$^{\alpha}$, C′) of all residues is shown in Fig. 5*B*.

MMP23$_{TxD}$ Shares Structural Similarity with BgK and ShK—Fig. 6*A* compares the closest to average structure of MMP23$_{TxD}$ with those of BgK and ShK. The location of several charged side chains on the molecular surface of MMP23$_{TxD}$ is highlighted in Fig. 6*B*. The backbone heavy atoms of the final 20 structures of MMP23$_{TxD}$ are superimposed over the final ensembles of BgK and ShK structures in Fig. 6, *C* and *D*, and the pairwise r.m.s. deviation values over the backbone heavy atoms between the structures of MMP23$_{TxD}$, BgK, and ShK are shown in Table 1. MMP23$_{TxD}$ shares greater structural similarity with BgK (r.m.s. deviation 2.28 Å) than ShK (2.77 Å). In fact, the structural similarity between MMP23$_{TxD}$ and BgK is greater than that of BgK and ShK (r.m.s. deviation 2.78 Å). MMP23$_{TxD}$, BgK and ShK have a turn involving the fifth cysteine residue (Cys^{30} in MMP23$_{TxD}$); this is followed by a short α-helix (residues 31–34) in MMP23$_{TxD}$ and BgK but not in ShK. The main differences between MMP23$_{TxD}$ and BgK are in the length of the first two helices, with the first helix in MMP23$_{TxD}$ being shorter and the second longer than in BgK.

MMP23$_{TxD}$ Exhibits Greater Structural Similarity to BgK Than the CRISP-ICR Domains—We compared the structure of MMP23$_{TxD}$ with that of the CRISP-ICR domains (13, 46–50) based on a backbone alignment of matching residues in a multiple alignment (Fig. 7 and Table 1). The ICR domains of snake (stecrisp, natrin, triflin, and pseudechetoxin) and human (CRISP-2/Tpx-1) CRISPs showed considerable structural sim-

ilarity (Fig. 7*A*). Among the snake proteins, the pairwise r.m.s. deviation values over the backbone heavy atoms ranged from 0.52 to 0.98 Å, and between the snake proteins and human CRISP-2/Tpx-1, the r.m.s. deviation was 0.98–1.32 Å (Table 1). Comparing the ICR domain structure of stecrisp as a representative of the CRISPs with the closest to average structure of $MMP23_{TxD}$ (Fig. 7*B*), the main differences were in the first and third loops (corresponding to residues 4–9 and 24–28 of $MMP23_{TxD}$), possibly because $MMP23_{TxD}$ has two fewer residues in the first loop and two more in the third loop (Fig. 2, *B* and *C*). Compared with BgK, the backbone of $MMP23_{TxD}$ aligned relatively well throughout, with the exception of the N-terminal region (Fig. 7*C*). The pairwise r.m.s. deviation values between the five ICR domains and $MMP23_{TxD}$ ranged from 2.98 to 3.07 Å. These ICR domains of CRISPs also showed less structural similarity to the sea anemone toxins BgK (r.m.s. deviations 2.97–3.09 Å) and ShK (r.m.s. deviations 3.53–3.79 Å) (Fig. 7 and Table 1). These structural results, together with the phylogenetic data demonstrate that $MMP23_{TxD}$s and sea anemone toxins share a closer relationship with each other than with ICR domains of CRISPs.

$MMP23_{TxD}$ Blocks Potassium Channels—BgK and ShK block Kv1.1, Kv1.3, Kv1.4, Kv1.6, Kv3.2, and KCa3.1 channels (15, 16, 51–55). We examined whether $MMP23_{TxD}$ also blocked these channels. The human Kv1.6 channel expressed in COS7 cells was blocked by $MMP23_{TxD}$ with a Hill coefficient approximating unity and an IC_{50} value of 370 nM (Fig. 8, *A*, *C*, and *D*). $MMP23_{TxD}$ also blocked Kv1.3 stably expressed in L929 fibroblasts (Fig. 8, *B–D*) and the Kv1.3 channel in human T cells (data not shown) with an IC_{50} value of 2.7 μM. A functional dyad composed of a critical lysine and an aromatic residue separated by 5–7 Å is present in many K^+ channel-blocking toxins (16), and the presence of

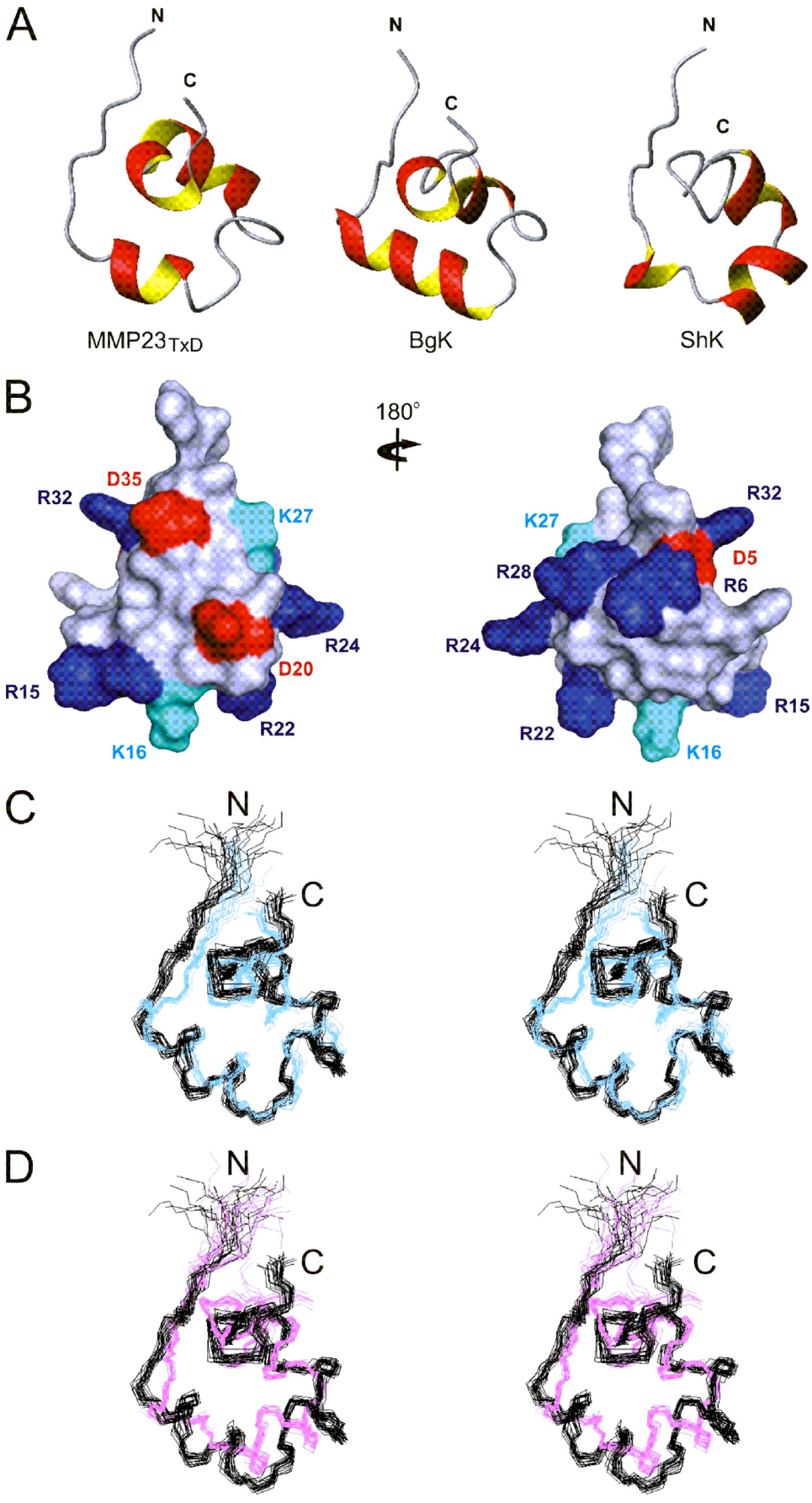

TABLE 1

Pairwise r.m.s. deviation over the backbone heavy atoms (N, C^{α}, C′) of $MMP23_{TxD}$, BgK, and ICR domains of CRISP proteins

Proteins shown are as follows: 1, stecrisp (Protein Data Bank code 1RC9); 2, $MMP23_{TxD}$; 3, natrin (Protein Data Bank code 1XTA); 4, pseudechetoxin (Protein Data Bank code 2DDA); 5, CRISP2/Tpx-1 (Protein Data Bank code 2A05); 6, BgK (Protein Data Bank code 1BGK); 7, ShK (Protein Data Bank code 1ROO); 8, triflin (Protein Data Bank code 1WVR). A total of 30 residues were used in the alignment to generate the r.m.s. deviation values. The residues used in the analysis include the following: stecrisp (184–189, 192–196, and 201–215), $MMP23_{TxD}$ (4–9, 10–14, 19–27, 30–34, and 36), Natrin (184–189, 192–196, and 201–215), pseudechetoxin (174–179, 182–186, and 191–205), triflin (184–189, 192–196, and 201–215), CRISP2/Tpx-1 (206–211, 214–218, and 223–237), BgK (3–8,11–15, 20–28, 30–34, and 36), ShK (4–9, 12–25, 28–32, and 34).

	1	2	3	4	5	6	7	8
1		3.07	0.77	0.82	1.13	3.09	3.79	0.52
2	3.07		3.06	2.98	3.05	2.28	2.77	2.99
3	0.77	3.06		0.75	1.07	3.11	3.57	0.81
4	0.82	2.98	0.75		1.32	2.97	3.53	0.98
5	1.13	3.05	1.07	1.32		3.08	3.60	0.98
6	3.09	2.28	3.11	2.97	3.08		2.78	3.06
7	3.79	2.77	3.57	3.53	3.60	2.78		3.71
8	0.52	2.99	0.81	0.98	0.98	3.06	3.71	

Arg^{24} and Leu^{25} in place of this dyad in $MMP23_{TxD}$ may contribute to its lower potency. However, the introduction of the dyad into $MMP23_{TxD}$ (Arg^{24}-Leu^{25} → Lys^{24}-Tyr^{25}) did not improve potency of $MMP23_{TxD}$ for Kv1.3 (IC_{50} 2.7 ± 0.5 μM). $MMP23_{TxD}$ exhibited lower affinity for Kv1.1, Kv3.2, and Kv1.4, whereas Kv1.5, Kv1.7, and KCa3.1 were unaffected by a 100 μM concentration of the peptide (Fig. 8, *B–D*).

Scorpion and sea anemone peptide toxins interact with a binding site in the outer vestibule of K^+ channels (1, 2, 52, 53). Toxin affinity for the binding site in Kv1.3 can be decreased either by titrating His^{404} at the entrance to the pore by lowering the external pH to 6.0 or by occupying the potassium-binding site in the ion selectivity filter by increasing the external K^+ concentration (1, 52, 53). Both of these manipulations destabilize the toxin channel interaction via electrostatic repulsion of the pore-occluding lysine (Lys^{27} in kaliotoxin and Lys^{22} in ShK) (1, 52, 53). We applied both of these tests to $MMP23_{TxD}$. Increasing external K^+ concentration or pH titration of His^{404} in Kv1.3 both significantly decreased $MMP23_{TxD}$s affinity for the channel (data not shown). These results suggest that $MMP23_{TxD}$ interacts with the external vestibule of Kv1.3.

Full-length MMP23 Suppresses K^+ Channels—Because $MMP23_{TxD}$ lies between the metalloprotease and the IgCAM domains in MMP23, it may not be optimally positioned in the full-length protein to block K^+ channels. To test whether $MMP23_{TxD}$ retained K^+ channel-blocking activity in full-length MMP23, N-terminal eGFP-tagged MMP23 (eGFP-MMP23) or eGFP was co-expressed in mammalian cells with $MMP23_{TxD}$-sensitive or -resistant channels. Confocal microscopy and patch clamp experiments were performed 30 h later. eGFP-MMP23 co-localized with $MMP23_{TxD}$-sensitive Kv1.3 channels (Fig. 9, *A* and *B*). In contrast, MMP23 did not co-localize with $MMP23_{TxD}$-resistant Kv1.2 channels (Fig. 9, *A* and *B*). eGFP did not co-localize with either channel (Fig. 9, *A* and *B*). These results suggest that $MMP23_{TxD}$ is required for MMP23 channel co-localization, although other domains in MMP23 may also contribute.

Published cell fractionation and confocal studies demonstrate that full-length MMP23 is an intracellular protein that is expressed primarily in ER/Golgi membranes (21, 22). We verified these results in our system by demonstrating that eGFP-MMP23, but not eGFP, co-localized with the ER membrane marker SERCA-2 (Fig. 9*C*). Because MMP23 is a type II transmembrane ER protein (21, 22), $MMP23_{TxD}$ will lie within the ER lumen, where it has the potential to bind to the outer vestibule of TxD-sensitive channels (Fig. 10*A*). Once compartmentalized with a $MMP23_{TxD}$-sensitive channel, the diffusion of MMP23 away from the channel is likely to be constrained by the ER membrane. Such an interaction might trap $MMP23_{TxD}$-sensitive channels in the ER and thereby decrease surface channel expression. In contrast, $MMP23_{TxD}$-resistant channels should be unaffected.

We performed two types of experiments to test for ER trapping. First, we performed whole-cell patch clamp experiments on cells co-expressing MMP23 and either $MMP23_{TxD}$-sensitive or -resistant channels. MMP23 suppressed $MMP23_{TxD}$-sensitive Kv1.6 and Kv1.3 currents but had no effect on $MMP23_{TxD}$-resistant Kv1.2 and Kv1.7 currents (Fig. 10*B*). These results indicate that fewer functional Kv1.3 channels are expressed in the surface cell membrane. Second, we used fluoresceinated ShK (ShK-F6CA) in flow cytometry experiments to measure cell surface protein expression of Kv1.3 in COS7 cells expressing Kv1.3 and either pDSRED-MMP23 or the control pDSRED-C1 monomer. ShK-F6CA (44) is a highly specific Kv1.3 inhibitor that blocks the channel (IC_{50} value 48 pM) 56,000-fold more potently than $MMP23_{TxD}$. The intensity of ShK-F6CA staining reflects the number of Kv1.3 tetramers on the cell surface because the peptide binds to the channel tetramer (44). Cell surface Kv1.3 expression was significantly lower in pDSRED-MMP23-expressing cells compared with pDSRED-C1-expressing controls (Fig. 10*C*). Taken together, these results suggest that MMP23 reduces surface expression of $MMP23_{TxD}$-sensitive Kv1.6 and Kv1.3 channels via intracellular trapping.

DISCUSSION

K^+ channels constitute the most abundant and diverse family of ion channels, and they regulate a myriad of functions in both excitable and non-excitable cells. Peptide toxins have helped to define the molecular mechanisms underlying K^+ channel function and to determine the relationship between K^+ currents in native tissues and specific genes. The cnidarian

FIGURE 6. **Comparison of structures of $MMP23_{TxD}$ and sea anemone K^+ channel blockers.** *A*, closest to average structure of $MMP23_{TxD}$ displayed in *ribbon form* using MolMol to depict the secondary structure and compared with that of BgK (Protein Data Bank 1BGK) and ShK (Protein Data Bank 1ROO). *N* and *C*, N and C termini, respectively. *B*, surface representation of $MMP23_{TxD}$ generated using PyMOL. The surface is *colored* with basic residues in *blue* (Arg in *dark blue* and Lys in *light blue*) and acidic residues in *red*. The two views are related by a 180° rotation about the vertical axis. *C*, stereo view of $MMP23_{TxD}$ (*black*) superimposed with BgK (*blue*) over backbone heavy atoms over aligned and well defined residues (residues 4–9, 10–28, and 30–36 for $MMP23_{TxD}$ with residues 3–8, 11–29, and 30–36 for BgK) (group global r.m.s. deviation 2.13 Å). *D*, stereo view of $MMP23_{TxD}$ (*black*) superimposed with ShK (*purple*) over backbone heavy atoms (residues 4–9, 10–14, and 19–36 for $MMP23_{TxD}$ with residues 4–9, 12–16, and 17–34 of ShK) (group global r.m.s. deviation 2.67 Å). Group global r.m.s. deviations are calculated from average pairwise r.m.s. deviations between each ensemble of final structures.

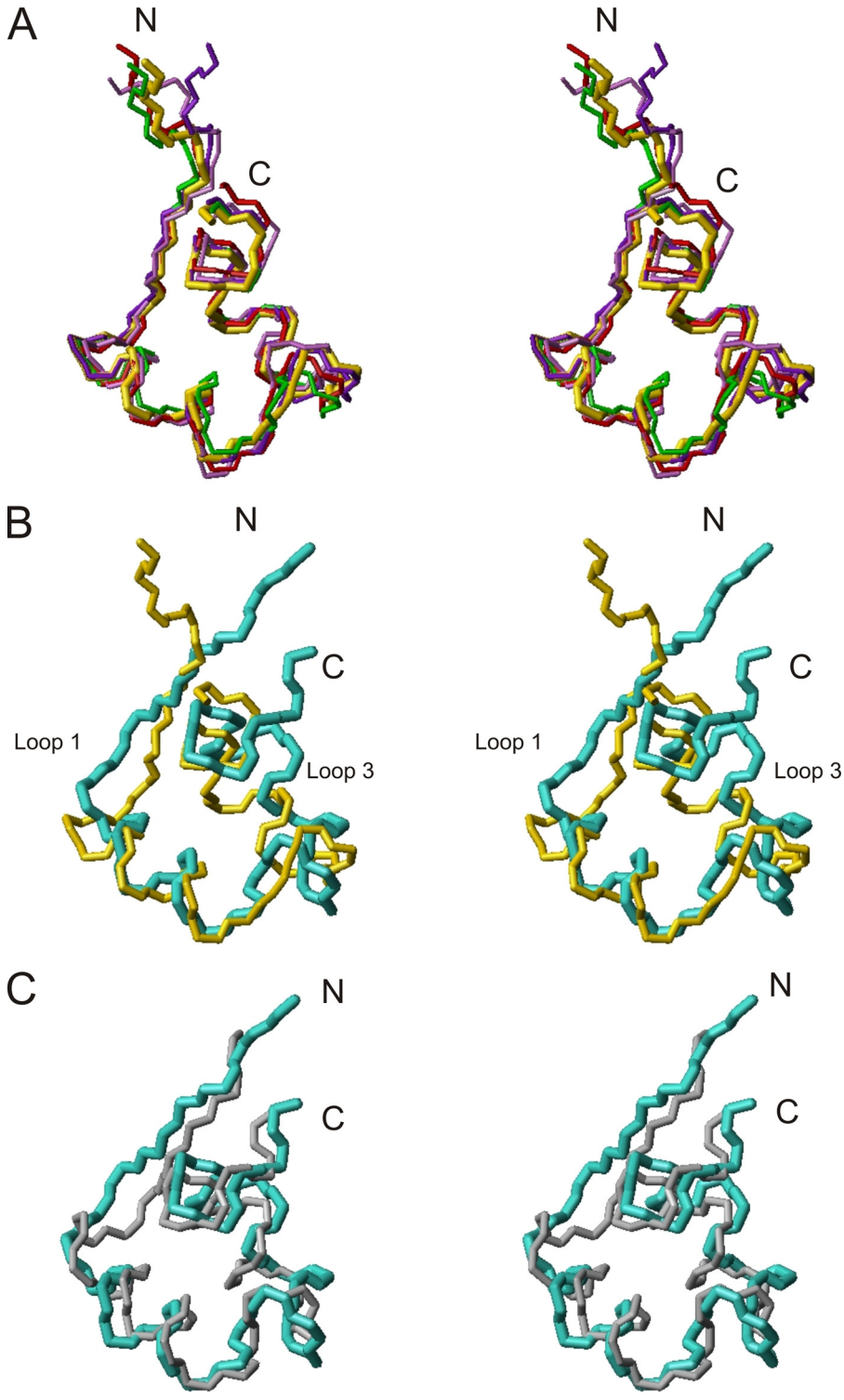

FIGURE 7. **Comparison with CRISP domain structures.** *A*, superposition of CRISP domains: stecrisp (*yellow*) (Protein Data Bank code 1RC9), natrin (*red*) (Protein Data Bank code 1XTA), triflin (*purple*) (Protein Data Bank code 1WVR), CRISP-2/Tpx-1 (*violet*) (Protein Data Bank code 2A05), and PsTx (*green*) (Protein Data Bank code 2DDA). *N* and *C*, N and C termini, respectively. *B*, superposition of closest to average structure of $MMP23_{TxD}$ (*light blue*) and stecrisp (*yellow*) (global r.m.s. deviation 3.07 Å). *C*, superposition of closest to average structure of $MMP23_{TxD}$ (*light blue*) and BgK (*gray*) (global r.m.s. deviation 2.28 Å). In all cases, structures were superimposed over backbone heavy atoms.

toxins ShK and BgK are potent inhibitors of voltage-gated and calcium-activated K^+ channels (15, 16, 51–55). SMART has identified domains in a vast number of proteins that resemble ShK and BgK (see the SMART Web site). A majority of these proteins are metallopeptidases belonging to the astacin/adamalysin family in *C. elegans* (Fig. 1). The three-dimensional structures and biological activities of these putative channel-blocking domains have not been determined. Because MMP23 is the only protein in humans identified by the SMART data base to contain such a domain, we have investigated the structure and physiological function of this domain.

$MMP23_{TxD}$s from diverse species exhibit a high degree of sequence conservation (Fig. 2*A*). They are evolutionarily related to the sea anemone toxins and to TxDs in a number of worm, cnidarian, and plant proteins and the ICR domains of snake and human CRISPs (Fig. 2*C*). Interestingly, we have found a second human protein (MFAP2), not included in the SMART data base, that contains a ShKT domain phylogenetically related to $MMP23_{TxD}$. MFAP2 is a matrix protein, which, like MMP23, is located on human chromosome 1p36 (45). The evolutionary relatedness of $MMP23_{TxD}$s is supported by the similarity of their three-dimensional structures. $MMP23_{TxD}$ and the sea anemone toxins share greater structural similarity with each other than with ICR domains; the structure of $MMP23_{TxD}$ is most similar to that of BgK (Figs. 5–7 and Table 1).

$MMP23_{TxD}$s and ICR domains are each encoded by a single exon (supplemental Fig. S1), suggesting that these two related structural motifs possibly arose from an ancient exon. In venomous creatures, this ancient module may have been modified to give rise to potent ion channel blockers, whereas the incorporation of this exon into plant oxidoreductases and prolyl hydroxylases and into worm astacin-like metalloproteases and trypsin-like serine proteases produced enzymes with potential channel-modulatory activity.

A lysine residue in sea anemone toxins (BgK^{25}, ShK^{22}) protrudes into and plugs the K^+ channel pore (15, 16, 51–55). $MMP23_{TxD}$s in opossum, chicken, zebra finch, and stickleback fish contain lysine at the corresponding position and should

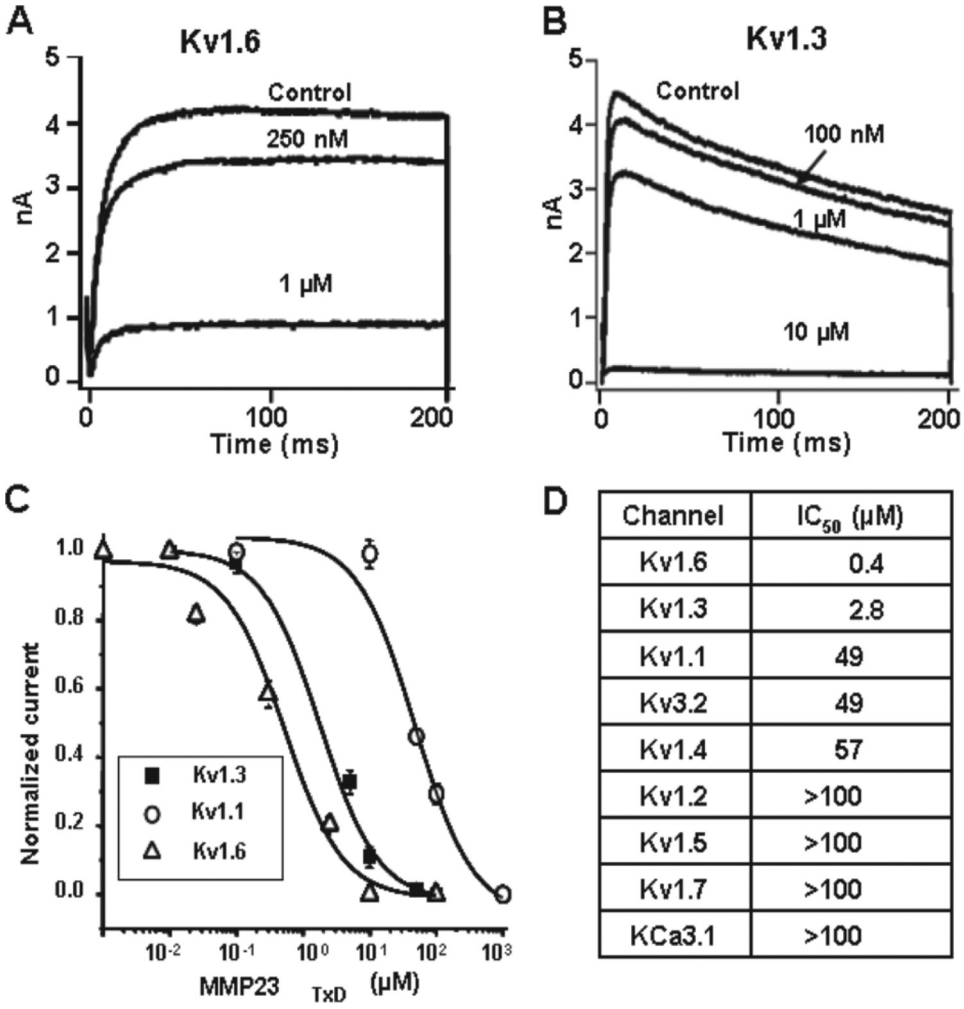

Channel	IC_{50} (μM)
Kv1.6	0.4
Kv1.3	2.8
Kv1.1	49
Kv3.2	49
Kv1.4	57
Kv1.2	>100
Kv1.5	>100
Kv1.7	>100
KCa3.1	>100

FIGURE 8. **$MMP23_{TxD}$ blocks Kv1.3 channels.** *A*, whole-cell patch clamp Kv1.6 current trace showing dose-dependent block of Kv1.6 channels by $MMP23_{TxD}$. *B*, whole-cell patch clamp Kv1.3 current trace showing dose-dependent block of Kv1.3 channels by $MMP23_{TxD}$. *C*, dose-response curves for Kv1.3, Kv1.6, and Kv1.1 channels blocked by $MMP23_{TxD}$; $n = 3–5$ for each data point. *D*, *table* showing IC_{50} values ± S.D. for respective channel block; $n = 4–5$ for each value.

block K^+ channels. We have shown that rat $MMP23_{TxD}$ containing an arginine at the equivalent position blocks Kv channels (Kv1.6 > Kv1.3 > Kv1.1 = Kv3.2 > Kv1.4, in decreasing potency) in the nanomolar to low micromolar range but has no effect on Kv1.2, Kv1.5, Kv1.7, and KCa3.1 at 100 μM concentration. The ICR domain of the snake protein natrin contains the critical pore-plugging lysine, and natrin has been reported to block Kv1.3 (46). The ICR domains of the four mammalian CRISPs lack the pore-occluding lysine and therefore may not block K^+ channels; CRISP-2/Tpx-1 blocks ryanodine receptors (13).

Full-length MMP23 has been reported previously to be expressed mainly in ER/Golgi membranes (21, 22). We confirmed these results by demonstrating that MMP23 co-localizes with the ER membrane marker SERCA-2 in COS7 cells. Because MMP23 is a type II transmembrane protein, $MMP23_{TxD}$ will lie within the ER lumen and could snare and trap $MMP23_{TxD}$-sensitive channels in the ER. Three lines of evidence support this idea. First, MMP23 compartmentalizes with $MMP23_{TxD}$-sensitive Kv1.3 channels but not with $MMP23_{TxD}$-resistant Kv1.2 channels. Second, MMP23 suppresses $MMP23_{TxD}$-sensitive channels while sparing $MMP23_{TxD}$-resistant ones. These results indicate that $MMP23_{TxD}$ within the full-length MMP23 protein has sufficient accessibility to bind to and block K^+ channels. Third, MMP23 decreases cell surface expression of $MMP23_{TxD}$-sensitive Kv1.3 channels.

It has been suggested previously that the preponderance of Kv1 channel heterotetramers in many tissues is the result of Kv1 homotetramers being retained in the ER by an unknown protein containing a TxD that binds to a trafficking determinant in the outer vestibule of the channel (59–61). Vacher *et al.* (61) provided support for this idea by showing that heterologously overexpressed, ER-luminal dendrotoxin competed with the TxD-containing ER protein for toxin-sensitive Kv1.1 homotetramers and allowed these channels to escape the ER and migrate to the plasma membrane. MMP23 fits the criteria for this ER protein because it contains a TxD that can trap sensitive Kv1 channels intracellularly. MMP23 is expressed in many tissues (lung, heart, uterus, placenta, ovary, testis seminiferous tubules, prostate, intestine, colon, pancreatic islets, cingulate cortex, adrenal cortex, osteoblasts, chondroblasts, cartilage, synovium, natural killer cells, dendritic cells, and tendons) (20, 23, 63–66) (see the BioGPS Web site) that overlap with the tissue expression of MMP23-sensitive K^+ channels. Therefore, there is a reasonable likelihood that MMP23 will modulate K^+ channels *in vivo*.

Our results for MMP23 help shed light on the vast family of proteins containing ShKT domains. Most of these proteins are found in *C. elegans*, many with multiple repeats of the domain in a single protein (Fig. 1). The ShKT domain in Mab7 is required for Mab7-mediated regulation of morphogenesis of sensory rays of the male *C. elegans* (56). The rays of Mab7-deficient males are virtually all malformed (56). Full-length Mab7, but not deletion constructs lacking the ShKT domain, rescues the abnormal phenotype (56). Because the *C. elegans* genome contains almost as many K^+ channel genes (~70) as humans, modulation of worm ion channels by the Mab7-ShKT domain could contribute to its role in morphogenesis. However, Mab7 lacks the critical pore-blocking positively charged residue, and a Mab7 hybrid construct containing the ShK toxin sequence in place of the TxD was not able to rescue the mutant ray phenotype (56). These findings suggest that the ShKT domain in Mab7 may not be involved in K^+ channel modulation, although modu-

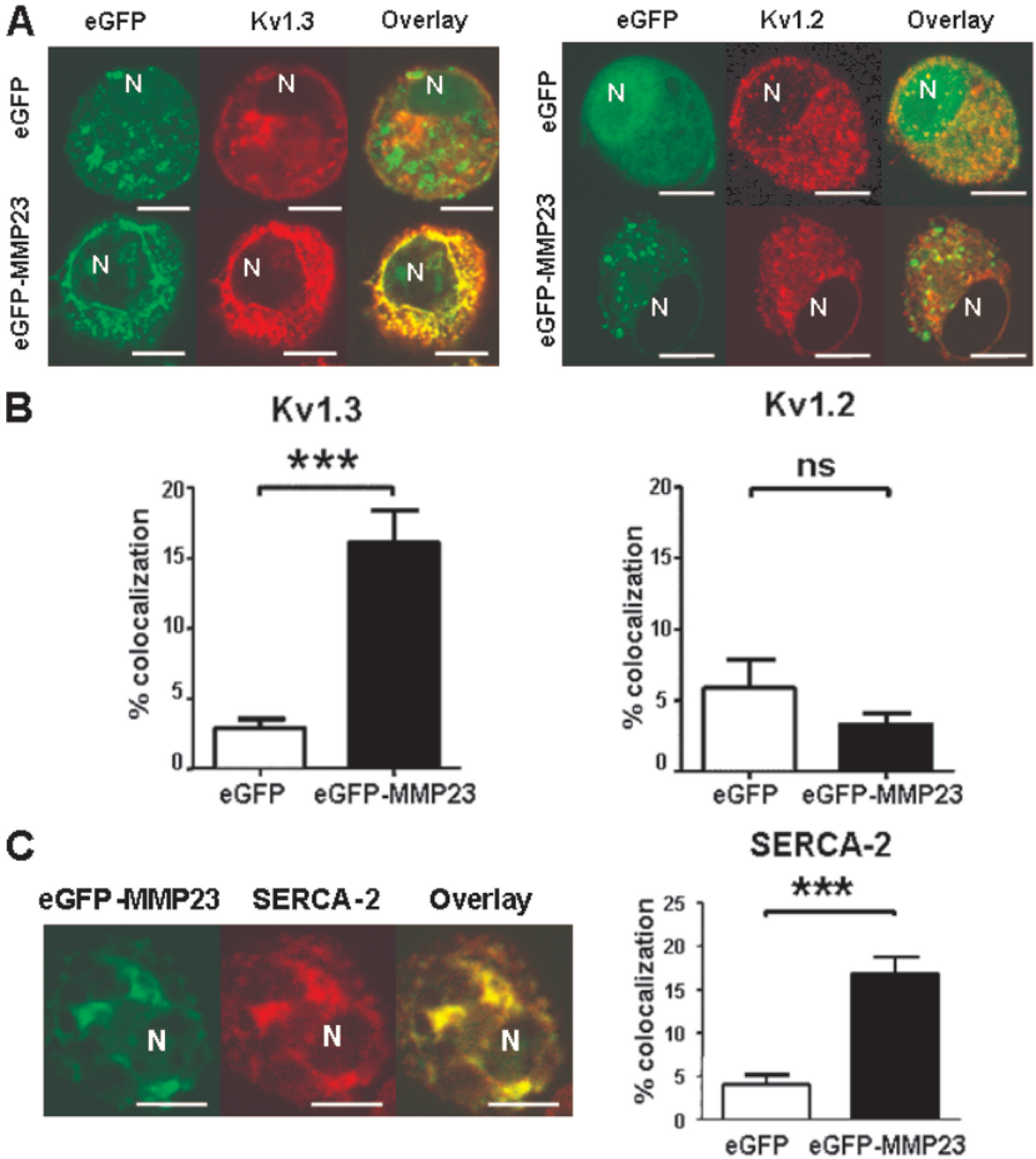

FIGURE 9. **MMP23 colocalizes with Kv1.3 in the ER.** MMP23 co-localizes with $MMP23_{TxD}$-sensitive Kv1 channels and with ER marker SERCA-2. *A*, eGFP-MMP23 (*green*) co-localizes with Kv1.3 channels (*red*) but not with Kv1.2 (*red*); eGFP did not co-localize with either channel. *B*, quantification of co-localization between eGFP or eGFP-MMP23 with Kv1.3 or Kv1.2 (*white bar*, $n = 25$ cells; *black bar*, $n = 30$ cells) (*, $p < 0.05$; **, $p < 0.01$; ***, $p < 0.001$; *ns*, not significant). *C*, eGFP-MMP23 (*green*) co-localizes with ER membrane marker SERCA-2 (*red*). Areas of co-localization are shown in *yellow* in the *overlay image*. eGFP does not co-localize with SERCA-2. *N*, nucleus.

lation of other types of ion channels cannot be excluded. Astacin-like metalloproteases in *Hydra vulgaris* (HMP2) and jellyfish (PMP1) possess ShKT domains that contain the critical pore-occluding lysine required for K^+ channel block, and both of these proteins play critical roles in foot morphogenesis (57, 58).

In summary, we have defined a novel channel-regulatory role for a metalloprotease and characterized the first functional K^+ channel-blocking toxin domain in a mammalian protein. Our results provide insight into the structure and function of the ShKT-containing protein superfamily. It is tempting to speculate that the TxDs in each of these proteins

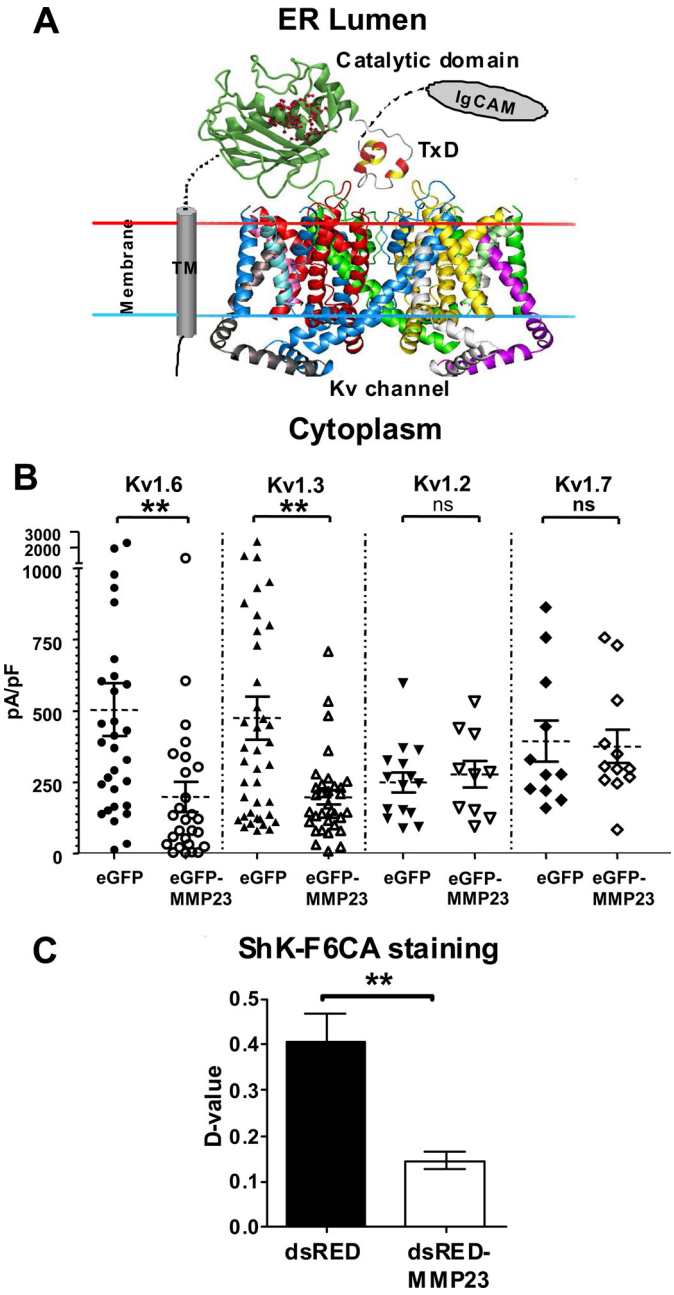

FIGURE 10. **Full-length MMP23 suppresses Kv1 channels by decreasing cell surface expression.** *A*, proposed orientation of MMP23 and Kv1 channels in the ER. The crystal structure of Kv1.2 (Protein Data Bank code 2a79) was used in this diagram because it is the only mammalian Kv1 channel for which a three-dimensional structure has been determined (62). Furthermore, its topology, particularly in the external vestibule where toxins bind, is similar to that of other Kv1 channels. In our depiction of MMP23, the transmembrane segment traverses the ER membrane; the metalloprotease domain (portrayed by the MMP3 catalytic domain structure, Protein Data Bank code 2jnp) lies within the ER lumen; and $MMP23_{TxD}$ is positioned in close proximity to the outer vestibule of the Kv1 channel. *B*, Kv1.6, Kv1.3, Kv1.2, and Kv1.7 current densities in the presence of eGFP (control) or eGFP-MMP23. Kv1.3 and Kv1.2 were stably expressed in L929-fibroblasts, whereas Kv1.6 and Kv1.7 were transiently expressed in COS7 cells. *Scatter diagrams* represent pooled data from 3–4 independent experiments. *, $p < 0.05$; **, $p < 0.01$; ***, $p < 0.001$; *ns*, not significant). *C*, pDSRED-MMP23 reduced ShK-F6CA staining of cell surface Kv1.3 channels as compared with pDSRED-C1 monomer in COS7 cells. The *D* value is a measure of the difference in fluorescence intensities of stained and unstained cells ($n = 5$ experiments, $p < 0.05$).

regulate different types of ion channels and that the evolutionary pressure to maintain channel-modulatory activity underlies the conservation of this domain throughout the plant and animal kingdoms.

Acknowledgments—We thank Dr. Michael Cahalan for valuable comments on the manuscript and Dr. Heike Wulff for the human Kv1.3 clone.

REFERENCES

1. Aiyar, J., Withka, J. M., Rizzi, J. P., Singleton, D. H., Andrews, G. C., Lin, W., Boyd, J., Hanson, D. C., Simon, M., Dethlefs, B., Gutman, G. A., and Chandy, K. G. (1995) *Neuron* **15,** 1169–1181
2. MacKinnon, R., Cohen, S. L., Kuo, A., Lee, A., and Chait, B. T. (1998) *Science* **280,** 106–109
3. Fry, B. G. (2005) *Genome Res.* **15,** 403–420
4. Ohno, M., Menez, R., Ogawa, T., Danse, J. M., Shimohigashi, Y., Fromen, C., Ducancel, F., Zinn-Justin, S., Le Du, M. H., Boulain, J. C., Tamiya, T., and Menez, A. (1998) *Prog. Nucleic Acids Res. Mol. Biol.* **59,** 307–364
5. Cousin, X., Bon, S., Massoulié, J., and Bon, C. (1998) *J. Biol. Chem.* **273,** 9812–9820
6. Davidson, F. F., and Dennis, E. A. (1990) *J. Mol. Evol.* **31,** 228–238
7. Kini, R. M., and Chan, Y. M. (1999) *J. Mol. Evol.* **48,** 125–132
8. Inoue, S., Oda, T., Koyama, J., Ikeda, K., and Hayashi, K. (1991) *FEBS Lett.* **279,** 38–40
9. Kochva, E., Bdolah, A., and Wollberg, Z. (1993) *Toxicon* **31,** 541–568
10. Ibañez-Tallon, I., Miwa, J. M., Wang, H. L., Adams, N. C., Crabtree, G. W., Sine, S. M., and Heintz, N. (2002) *Neuron* **33,** 893–903
11. Miwa, J. M., Ibanez-Tallon, I., Crabtree, G. W., Sánchez, R., Sali, A., Role, L. W., and Heintz, N. (1999) *Neuron* **23,** 105–114
12. Harvey, A. L., and Robertson, B. (2004) *Curr. Med. Chem.* **11,** 3065–3072
13. Gibbs, G. M., Scanlon, M. J., Swarbrick, J., Curtis, S., Gallant, E., Dulhunty, A. F., and O'Bryan, M. K. (2006) *J. Biol. Chem.* **281,** 4156–4163
14. Fry, B. G., Roelants, K., Champagne, D. E., Scheib, H., Tyndall, J. D., King, G. F., Nevalainen, T. J., Norman, J. A., Lewis, R. J., Norton, R. S., Renjifo, C., and de la Vega, R. C. (2009) *Annu. Rev. Genomics Hum. Genet.* **10,** 483–511
15. Cotton, J., Crest, M., Bouet, F., Alessandri, N., Gola, M., Forest, E., Karlsson, E., Castañeda, O., Harvey, A. L., Vita, C., and Ménez, A. (1997) *Eur. J. Biochem.* **244,** 192–202
16. Dauplais, M., Lecoq, A., Song, J., Cotton, J., Jamin, N., Gilquin, B., Roumestand, C., Vita, C., de Medeiros, C. L., Rowan, E. G., Harvey, A. L., and Ménez, A. (1997) *J. Biol. Chem.* **272,** 4302–4309
17. Castañeda, O., Sotolongo, V., Amor, A. M., Stöcklin, R., Anderson, A. J., Harvey, A. L., Engström, A., Wernstedt, C., and Karlsson, E. (1995) *Toxicon* **33,** 603–613
18. Tudor, J. E., Pallaghy, P. K., Pennington, M. W., and Norton, R. S. (1996) *Nat. Struct. Biol.* **3,** 317–320
19. Page-McCaw, A., Ewald, A. J., and Werb, Z. (2007) *Nat. Rev. Mol. Cell Biol.* **8,** 221–233
20. Velasco, G., Pendás, A. M., Fueyo, A., Knäuper, V., Murphy, G., and López-Otín, C. (1999) *J. Biol. Chem.* **274,** 4570–4576
21. Pei, D. (1999) *FEBS Lett.* **457,** 262–270
22. Pei, D., Kang, T., and Qi, H. (2000) *J. Biol. Chem.* **275,** 33988–33997
23. Ohnishi, J., Ohnishi, E., Jin, M., Hirano, W., Nakane, D., Matsui, H., Kimura, A., Sawa, H., Nakayama, K., Shibuya, H., Nagashima, K., and Takahashi, T. (2001) *Mol. Endocrinol.* **15,** 747–764
24. Riddick, A. C., Shukla, C. J., Pennington, C. J., Bass, R., Nuttall, R. K., Hogan, A., Sethia, K. K., Ellis, V., Collins, A. T., Maitland, N. J., Ball, R. Y., and Edwards, D. R. (2005) *Br. J. Cancer* **92,** 2171–2180
25. Hegedüs, L., Cho, H., Xie, X., and Eliceiri, G. L. (2008) *J. Cell Physiol.* **216,** 480–485
26. Scrideli, C. A., Carlotti, C. G., Jr., Okamoto, O. K., Andrade, V. S., Cortez, M. A., Motta, F. J., Lucio-Eterovic, A. K., Neder, L., Rosemberg, S., Oba-Shinjo, S. M., Marie, S. K., and Tone, L. G. (2008) *J. Neurooncol.* **88,**

281–291
27. King, D. S., Fields, C. G., and Fields, G. B. (1990) *Int. J. Pept. Protein Res.* **36,** 255–266
28. Palmer, A. G., Cavanagh, J., Wright, P. E., and Rance, M. (1991) *J. Magn. Reson.* **93,** 151–170
29. Piotto, M., Saudek, V., and Sklenár, V. (1992) *J. Biomol. NMR* **2,** 661–665
30. Kay, L., Keifer, P., and Saarinen, T. (1992) *J. Am. Chem. Soc.* **114,** 10663–10665
31. Gibbs, S. J., and Johnson, Jr., C. S. (1991) *J. Magn. Reson*. **93,** 395–402
32. Dingley, A. J., Mackay, J. P., Chapman, B. E., Morris, M. B., Kuchel, P. W., Hambly, B. D., and King, G. F. (1995) *J. Biomol. NMR* **6,** 321–328
33. Yao, S., Howlett, G. J., and Norton, R. S. (2000) *J. Biomol. NMR* **16,** 109–119
34. Bartels, C., Xia, T. H., Billeter, M., Güntert, P., and Wüthrich, K. (1995) *J. Biomol. NMR* **6,** 1–10
35. Cornilescu, G., Delaglio, F., and Bax, A. (1999) *J. Biomol. NMR* **13,** 289–302
36. Seavey, B. R., Farr, E. A., Westler, W. M., and Markley, J. L. (1991) *J. Biomol. NMR* **1,** 217–236
37. Klaus, W., Broger, C., Gerber, P., and Senn, H. (1993) *J. Mol. Biol.* **232,** 897–906
38. Herrmann, T., Güntert, P., and Wüthrich, K. (2002) *J. Biomol. NMR* **24,** 171–189
39. Schwieters, C. D., Kuszewski, J. J., Tjandra, N., and Clore, G. M. (2003) *J. Magn. Reson*. **160,** 65–73
40. Laskowski, R. A., Rullmannn, J. A., MacArthur, M. W., Kaptein, R., and Thornton, J. M. (1996) *J. Biomol. NMR* **8,** 477–486
41. Koradi, R., Billeter, M., and Wüthrich, K. (1996) *J. Mol. Graph.* **14,** 51–55
42. Berman, H. M., Battistuz, T., Bhat, T. N., Bluhm, W. F., Bourne, P. E., Burkhardt, K., Feng, Z., Gilliland, G. L., Iype, L., Jain, S., Fagan, P., Marvin, J., Padilla, D., Ravichandran, V., Schneider, B., Thanki, N., Weissig, H., Westbrook, J. D., and Zardecki, C. (2002) *Acta Crystallogr. D Biol. Crystallogr.* **58,** 899–907
43. Beeton, C., Smith, B. J., Sabo, J. K., Crossley, G., Nugent, D., Khaytin, I., Chi, V., Chandy, K. G., Pennington, M. W., and Norton, R. S. (2008) *J. Biol. Chem.* **283,** 988–997
44. Beeton, C., Wulff, H., Singh, S., Botsko, S., Crossley, G., Gutman, G. A., Cahalan, M. D., Pennington, M., and Chandy, K. G. (2003) *J. Biol. Chem.* **278,** 9928–9937
45. Faraco, J., Bashir, M., Rosenbloom, J., and Francke, U. (1995) *Genomics* **25,** 630–637
46. Wang, F., Li, H., Liu, M. N., Song, H., Han, H. M., Wang, Q. L., Yin, C. C., Zhou, Y. C., Qi, Z., Shu, Y. Y., Lin, Z. J., and Jiang, T. (2006) *Biochem. Biophys. Res. Commun.* **351,** 443–448
47. Guo, M., Teng, M., Niu, L., Liu, Q., Huang, Q., and Hao, Q. (2005) *J. Biol. Chem.* **280,** 12405–12412
48. Shikamoto, Y., Suto, K., Yamazaki, Y., Morita, T., and Mizuno, H. (2005) *J. Mol. Biol.* **350,** 735–743
49. Suzuki, N., Yamazaki, Y., Fujimoto, Z., Morita, T., and Mizuno, H. (2005) *Acta Crystallogr. Sect. F Struct. Biol. Cryst. Commun.* **61,** 750–752
50. Wang, J., Shen, B., Guo, M., Lou, X., Duan, Y., Cheng, X. P., Teng, M., Niu, L., Liu, Q., Huang, Q., and Hao, Q. (2005) *Biochemistry* **44,** 10145–10152
51. Tudor, J. E., Pennington, M. W., and Norton, R. S. (1998) *Eur. J. Biochem.* **251,** 133–141
52. Kalman, K., Pennington, M. W., Lanigan, M. D., Nguyen, A., Rauer, H., Mahnir, V., Paschetto, K., Kem, W. R., Grissmer, S., Gutman, G. A., Christian, E. P., Cahalan, M. D., Norton, R. S., and Chandy, K. G. (1998) *J. Biol. Chem.* **273,** 32697–32707
53. Rauer, H., Pennington, M., Cahalan, M., and Chandy, K. G. (1999) *J. Biol. Chem.* **274,** 21885–21892
54. Alessandri-Haber, N., Lecoq, A., Gasparini, S., Grangier-Macmath, G., Jacquet, G., Harvey, A. L., de Medeiros, C., Rowan, E. G., Gola, M., Ménez, A., and Crest, M. (1999) *J. Biol. Chem.* **274,** 35653–35661
55. Gilquin, B., Racapé, J., Wrisch, A., Visan, V., Lecoq, A., Grissmer, S., Ménez, A., and Gasparini, S. (2002) *J. Biol. Chem.* **277,** 37406–37413
56. Tsang, S. W., Nguyen, C. Q., Hall, D. H., and Chow, K. L. (2007) *Dev. Biol.* **312,** 353–366
57. Yan, L., Fei, K., Zhang, J., Dexter, S., and Sarras, M. P., Jr. (2000) *Development* **127,** 129–141
58. Pan, T., Gröger, H., Schmid, V., and Spring, J. (1998) *Dev. Genes Evol.* **208,** 259–266
59. Manganas, L. N., Wang, Q., Scannevin, R. H., Antonucci, D. E., Rhodes, K. J., and Trimmer, J. S. (2001) *Proc. Natl. Acad. Sci. U.S.A.* **98,** 14055–14059
60. Zhu, J., Watanabe, I., Gomez, B., and Thornhill, W. B. (2001) *J. Biol. Chem.* **276,** 39419–39427
61. Vacher, H., Mohapatra, D. P., Misonou, H., and Trimmer, J. S. (2007) *FASEB J.* **21,** 906–914
62. Long, S. B., Campbell, E. B., and Mackinnon, R. (2005) *Science* **309,** 897–903
63. Fortunato, S. J., and Menon, R. (2002) *J. Assist. Reprod. Genet.* **19,** 483–486
64. Clancy, B. M., Johnson, J. D., Lambert, A. J., Rezvankhah, S., Wong, A., Resmini, C., Feldman, J. L., Leppanen, S., and Pittman, D. D. (2003) *Bone* **33,** 46–63
65. Davidson, R. K., Waters, J. G., Kevorkian, L., Darrah, C., Cooper, A., Donell, S. T., and Clark, I. M. (2006) *Arthritis Res. Ther.* **8,** R124
66. Jones, G. C., Corps, A. N., Pennington, C. J., Clark, I. M., Edwards, D. R., Bradley, M. M., Hazleman, B. L., and Riley, G. P. (2006) *Arthritis Rheum.* **54,** 832–842